

On the Quasilinear Saturation of the Parallel Proton Firehose Instability Using a Full-f Approach

Patrick Astfalk¹, Frank Jenko¹

¹Max-Planck-Institut für Plasmaphysik, Boltzmannstrasse 2, 85748 Garching, Germany.

Key Points:

- We apply kinetic quasilinear theory to firehose saturation using a full-f approach.
- We compare with moment-kinetic approach and hybrid-kinetic simulations.
- The employed full-f approach gives good results as long as initial firehose growth is not too strong.

Corresponding author: Patrick Astfalk, patrick.astfalk@ipp.mpg.de

Abstract

A classic example for the application of quasilinear theory to electromagnetic wave-particle interactions, the saturation of the parallel proton firehose instability, is usually considered in the long-wavelength approximation although for $\beta_{\parallel,p} \lesssim 25$ this instability is dominated by anomalous cyclotron resonance which invalidates a macroscopic treatment [Gary *et al.*, 1998]. To relax the long-wavelength approximation, Seough *et al.* [2015] solved the microscopic weak turbulence kinetic equation to model the temperature anisotropy reduction of the firehose also in the resonant regime. However, the employed moment-kinetic approach assumes the preservation of the initially bi-Maxwellian shape of the underlying proton velocity distribution throughout the saturation process, leading to poor results for low $\beta_{\parallel,p}$. In this work, we lift the limitations of the moment-kinetic approach and we demonstrate that allowing for distribution deformation due to anomalous cyclotron-resonant scattering greatly improves the predictions of the kinetic quasilinear model except for cases of very strong firehose growth. We conclude that quasilinear theory can be a valid model for studying the parallel firehose saturation even in the strongly cyclotron-resonant regime as long as the initial temperature anisotropy is not too large.

1 Introduction

Due to its low collisionality, the solar wind medium can easily develop and maintain significant temperature anisotropies, providing a source of free energy which may drive various kinetic instabilities. From spacecraft measurements, it has long been known that the temperature anisotropies observed in the solar wind are clearly constrained to a certain parameter space whose bounds are identified as signatures of active instabilities [Gary *et al.*, 2001; Kasper *et al.*, 2002; Bale *et al.*, 2009]. As soon as the anisotropy of the plasma locally exceeds a certain threshold, an instability is excited which will act to isotropize the plasma, hence preventing the temperature from becoming even more anisotropic and keeping the plasma at a marginally stable state.

For anisotropies $T_{\perp,p} > T_{\parallel,p}$, the proposed instability mechanisms are the electromagnetic ion cyclotron (EMIC) instability, which is propagating parallel to the background magnetic field with finite frequency, and the mirror instability which is purely growing and has $k_{\perp} \neq 0$ (see, e.g., Sagdeev and Shafranov [1961]; Gary and Lee [1994]; Southwood and Kivelson [1993] and references therein). The opposite anisotropy, $T_{\parallel,p} > T_{\perp,p}$, can drive the parallel proton firehose instability (PFHI) which has finite frequency, and the oblique firehose (OFHI) which – similar to the mirror instability – is non-propagating and only grows for $\theta > 0^\circ$ (see, e.g., Quest and Shapiro [1996]; Gary *et al.* [1998]; Hellinger and Matsumoto [2000] and references therein).

Marginal stability conditions of these instabilities have been derived from linear kinetic theory and have been used to fit the bounds of the observed proton temperature anisotropies in the solar wind [Hellinger *et al.*, 2006]. For $\beta_{\parallel,p} \gg 1$, a good match is found with the firehose and the mirror thresholds in the fluid approximation. The agreement with the fluid threshold even improves when also accounting for electron and minor ion temperature anisotropies [Chen *et al.*, 2016]. However, for $\beta_{\parallel,p} \sim \mathcal{O}(1)$, the observed anisotropy bounds in the $T_{\parallel,p} > T_{\perp,p}$ regime do not match the linear predictions for the two firehose modes. Moreover, for $\beta_{\parallel,p} \gtrsim 2$ the anisotropy boundary roughly follows the oblique firehose threshold although the PFHI is more easily excited when $\beta_{\parallel,p} < 10$. Similarly, in the $T_{\perp,p} > T_{\parallel,p}$ regime, the anisotropies seem to follow the mirror instability threshold although the EMIC instability should be active at significantly lower anisotropies.

Understanding the apparent failure of the parallel propagating instabilities, EMIC and PFHI, to constrain proton temperature anisotropies in the solar wind, poses a challenge which still requires further investigation. Several solutions have been suggested to resolve this issue, such as the inclusion of electron temperature anisotropies [Michno *et al.*, 2014; Shaaban *et al.*, 2017] or minor ion anisotropies [Matteini *et al.*, 2012]. Yoon *et al.*

[2014] gives a concise review of possible explanations and puts forth another approach imposing a time-varying background magnetic field.

Isenberg et al. [2013] follows yet another path and argues that bi-Maxwellian distributions can never be stable with respect to cyclotron-resonant interactions. Thus, using bi-Maxwellian thresholds for the EMIC instability, which is strongly driven by cyclotron resonance, is misleading. Instead, the stable state is set by vanishing ion cyclotron resonant particle scattering, yielding a threshold which lies well above the mirror threshold, thus explaining the discrepancy in the solar wind data.

In line with the findings of *Isenberg et al.* [2013] for the EMIC instability, *Astfalk and Jenko* [2017] showed that in the low- $\beta_{\parallel,p}$ regime, the saturation of the parallel proton firehose growth is mainly driven by anomalous cyclotron-resonant diffusion and not by macroscopic temperature anisotropy reduction. Hence, the argument of *Isenberg et al.* [2013] applies to the PFHI as well which may explain why the PFHI apparently does not constrain the proton temperature anisotropy in the low- $\beta_{\parallel,p}$ regime in the solar wind. The purpose of this work is to further verify this claim and to shed more light on the temperature anisotropy reduction during the PFHI saturation.

In kinetic theory, the saturation and simultaneous temperature anisotropy reduction of the PFHI is usually modeled by means of quasilinear theory (QLT). The quasilinear firehose saturation in the long-wavelength limit is a standard textbook problem and has been explored extensively in the past [*Shapiro and Shevchenko*, 1964; *Davidson and Völk*, 1968; *Davidson*, 1972; *Yoon*, 1995]. A macroscopic treatment may give good estimates for the final temperature and energy saturation levels in the case of high $\beta_{\parallel,p}$. However, in the regime $\beta_{\parallel,p} \lesssim 25$ where the dynamics is dominated by cyclotron resonance [*Gary et al.*, 1998], it is not applicable. To lift the restrictions of the long-wavelength approximation, *Seough and Yoon* [2012] and *Seough et al.* [2015] followed a more general approach, termed *moment-kinetic theory* where the microscopic weak turbulence kinetic equation is employed to self-consistently evolve the temperature anisotropy of a firehose-unstable system in time while co-evolving the wave spectra generated by the instability. A comparison with fully-kinetic PIC simulations revealed that for $\beta_{\parallel,p} = 10$, the approach produces good agreement with the observed saturation levels while for $\beta_{\parallel,p} \sim \mathcal{O}(1)$ there is still a clear offset. *Seough et al.* [2015] proposed two possible explanations for this discrepancy:

(1) QLT does not include nonlinear wave-wave interactions. However, *Quest and Shapiro* [1996] found that strong wave-wave interactions can be present during the PFHI growth suppression which redistribute the energy in the wave spectrum and interfere with the quasilinear saturation.

(2) The chosen moment-based approach does not allow for a non-Maxwellian deformation of the initially bi-Maxwellian particle velocity distribution. It assumes that the distribution preserves its bi-Maxwellian shape throughout the saturation process while only its macroscopic temperature components $T_{\parallel,p}$, $T_{\perp,p}$ can change.

In light of the fact that *Seough et al.* [2015] report significant dumbbell-like deformation of the velocity distribution in PIC simulations which, in line with the findings of *Matteini et al.* [2006], gets more pronounced for decreasing $\beta_{\parallel,p}$, and accounting for the results of *Astfalk and Jenko* [2017] that anomalous cyclotron-resonant diffusion can play a crucial role in the growth suppression, we conclude that the latter of the two explanations asks for a careful inspection. To address this point, we embedded LEOPARD, a linear kinetic dispersion relation solver for arbitrary gyrotropic distributions [*Astfalk and Jenko*, 2017], in the kinetic quasilinear framework which allows us to relax the assumption of bi-Maxwellian preservation in the moment-kinetic approach. This new full-f approach enables the inclusion of effects due to distribution deformation caused by linear wave-particle interactions. We use this method to revisit the applicability of kinetic QLT to the saturation of the PFHI by examining the growth suppression in six exemplary PFHI setups.

The presented work is structured as follows. In section 2, we list the equations used in the quasilinear approach and briefly discuss their implementation in the new quasi-

linear solver QLEO. In section 3.1, we benchmark the QLEO code with results from a quasilinear moment-kinetic treatment. And in section 3.2, we compare the outcomes of our full-f quasilinear approach with the results of a moment-kinetic analysis and with 1D3V hybrid-kinetic simulations. Section 4 concludes the discussion.

2 Kinetic quasilinear theory and its implementation

Collisionless magnetized plasmas are able to carry a rich variety of kinetic eigenmodes which can be characterized by their corresponding kinetic dispersion relation $\omega(\mathbf{k})$. As long as the field amplitudes of the kinetic modes are small compared to the background fields, they are well described in the framework of linear kinetic theory. Linear dispersion relations provide information not only on the real frequency spectrum of the modes but also on their linear stability. If the plasma is not in thermal equilibrium, but a source of free energy is present, eigenmodes of the system eventually tap this source and their frequency acquires a positive imaginary part which is identified as the temporal growth rate $\gamma(\mathbf{k})$ of the mode – an instability occurs. However, it is obvious that the resulting exponential growth of the mode cannot proceed indefinitely. As soon as the amplitudes reach a certain magnitude, the assumptions of linear theory get invalidated and nonlinear physics may take over. Usually, the instability is self-destructive, i.e. it exhausts the energy source that feeds it. So, the transition from the linear stage of growth to the nonlinear regime goes hand in hand with the saturation of the linearly-unstable mode. The nonlinear regime is then dominated by nonlinear wave-particle and wave-wave interactions which pave the way for strong particle energization and the onset of turbulence.

The complexity of nonlinear kinetic physics hardly allows a thorough investigation of the underlying processes. However, to get insight into the saturation mechanism, a perturbative expansion can be used – the *weak turbulence kinetic theory* of wave-particle interactions which applies when the energy in the spectrum of excited modes is small compared to the total energy in the plasma. Accounting only for the zero- and first-order in the expansion, the so-called quasilinear model can be constructed which has been successfully applied to numerous microscopic and macroscopic instabilities. The underlying assumption of QLT can be found in many standard textbooks on kinetic plasma physics and shall not be discussed in depth here. We only note that this approach enables us to describe how the particle velocity distribution reacts to the initially unstable mode spectrum due to linear wave-particle interactions, ultimately leading to a stabilization of the parallel firehose-unstable system. Under the assumption of slow temporal changes, the time evolution of the distribution function can then be described by the parallel weak turbulence kinetic equation (see, e.g. *Davidson* [1972]) which, in normalized units, reads (for the protons):

$$\begin{aligned} \frac{\partial \tilde{f}_p}{\partial t} = & \operatorname{Re} \left(\frac{i}{4} \sum_{+,-} \int_{-\infty}^{\infty} d\tilde{k}_{\parallel} \left(\left(1 - \frac{\tilde{k}_{\parallel} \tilde{v}_{\parallel}}{\tilde{\omega}^*} \right) \frac{1}{\tilde{v}_{\perp}} \frac{\partial}{\partial \tilde{v}_{\perp}} + \frac{\tilde{k}_{\parallel}}{\tilde{\omega}^*} \frac{\partial}{\partial \tilde{v}_{\parallel}} \right) \times \right. \\ & \left. \frac{\delta \tilde{B}_k^2 |\tilde{\omega}|^2 / \tilde{k}_{\parallel}^2}{\tilde{\omega} \pm 1 - \tilde{k}_{\parallel} \tilde{v}_{\parallel}} \left(\left(1 - \frac{\tilde{k}_{\parallel} \tilde{v}_{\parallel}}{\tilde{\omega}} \right) \tilde{v}_{\perp} \frac{\partial \tilde{f}_p}{\partial \tilde{v}_{\perp}} + \frac{\tilde{k}_{\parallel} \tilde{v}_{\perp}^2}{\tilde{\omega}} \frac{\partial \tilde{f}_p}{\partial \tilde{v}_{\parallel}} \right) \right). \end{aligned} \quad (1)$$

The meaning of the quantities and the used normalizations and can be found in appendix A: . The sum $\sum_{+,-}$ runs over right-hand (+) and left-hand (−) polarized modes and * denotes complex conjugation. Please note that the wavenumber integral is to be understood as a principal value integral, since there are singularities in the integration interval. Moreover, Eq. 1 holds for growing modes only, i.e. $\operatorname{Im}(\tilde{\omega}) = \tilde{\gamma}_k > 0$, and has to be analytically continued accordingly when including damped modes with $\tilde{\gamma}_k \leq 0$, i.e. contributions from the poles have to be added in the usual way, following Landau's prescription (see, e.g., *Landau* [1946]).

The PFHI exhibits the fastest growth for parallel propagation but also grows for $\theta \neq 0$. However, Eq. 1 is restricted to parallel propagation, thus, effects due to higher dimensionality will not be included here.

Solving Eq. 1 requires knowledge of the temporal changes of the wave energy spectrum $\delta\tilde{B}_k^2$. It can be evolved in time according to:

$$\frac{\partial\delta\tilde{B}_k^2}{\partial t} = 2\tilde{\gamma}_k\delta\tilde{B}_k^2. \quad (2)$$

The new quasilinear solver QLEO solves this closed set of equations numerically, using an explicit Euler method where the velocity distribution is sampled on a two-dimensional velocity grid, $\tilde{v}_{\parallel} \times \tilde{v}_{\perp}$. The real frequency $\tilde{\omega}_k$ and the temporal growth rate $\tilde{\gamma}_k$, required in Eqs. 1 and 2, are constantly updated by feeding the distribution function into the dispersion relation solver LEOPARD at each time step.

For the evaluation of the wavenumber integral in Eq. 1, we refrained from performing a direct numerical integration. Instead, we implemented a more efficient method which can be briefly summarized as follows: At each time step, the frequency spectrum $\tilde{\omega}_k$, the growth rate spectrum $\tilde{\gamma}_k$, and the magnetic energy spectrum $\delta\tilde{B}_k^2$ are interpolated with natural cubic splines over the whole wavenumber range. This turns the integral into a piecewise rational function and allows a piecewise analytical evaluation of the integral. A pitfall here is that the denominator of the integrand, which turns into a cubic function of \tilde{k}_{\parallel} , can have zeros within the considered wavenumber interval. This introduces poles which have to be accounted for accordingly and may require analytic continuation. After evaluating the integral for each piece of the integration interval, its principal values and the contributions from the poles are simply added up. The integration is performed on an equidistant, adaptive grid which is adjusted at each time step to cover all unstable modes, ranging from the unstable mode with lowest \tilde{k}_{\parallel} to the unstable mode with highest \tilde{k}_{\parallel} .

The derivatives of the velocity distribution showing up in Eq. 1 are computed by employing a local exponential fit function which is more suitable than applying conventional central difference methods and gives better stability of the code.

To ensure symmetry, we always include back- and forward-propagating modes when evaluating the weak turbulence kinetic equation, picking out the right polarity for each case. The PFHI which destabilizes the whistler branch is driven by anomalous cyclotron resonance, hence it requires the presence of right-hand polarized whistler modes.

3 Application of the quasilinear full-f approach

3.1 Validation with moment-kinetic approach

In a series of papers, *Seough and Yoon* [2012]; *Seough et al.* [2014, 2015] applied kinetic QLT to study the saturation of the PFHI and the EMIC instability. One major assumption used in these studies was the preservation of the velocity distribution's bi-Maxwellian shape throughout the saturation process. This allowed for a moment-kinetic approach where only the macroscopic quantities β_{\parallel} and β_{\perp} , with $\beta = 8\pi n k_B T / B_0^2$, are advanced in time instead of evolving the full velocity distribution. The corresponding evolution equation for each beta component can be derived from the weak turbulence kinetic equation, Eq. 1, by replacing \tilde{f}_p with a bi-Maxwellian, i.e.

$$\tilde{f}_p = \frac{1}{\sqrt{\beta_{\parallel,p}}\beta_{\perp,p}} \exp\left(-\frac{\tilde{v}_{\parallel}^2}{\beta_{\parallel,p}} - \frac{\tilde{v}_{\perp}^2}{\beta_{\perp,p}}\right), \quad (3)$$

and by taking the second velocity moments $\langle \tilde{v}_{\parallel}^2 \cdot (...) \rangle$ and $\langle \tilde{v}_{\perp}^2 \cdot (...) \rangle$ of the whole expression, yielding

$$\begin{aligned} \frac{\partial \beta_{\parallel, \text{p}}}{\partial \tilde{t}} &= \text{Re} \left(-2i \sum_{+, -} \int_{-\infty}^{\infty} d\tilde{k}_{\parallel} \frac{\delta \tilde{B}_k^2}{\tilde{k}_{\parallel}^2} \left(\tilde{\omega} + \left(\frac{\beta_{\perp, \text{p}}}{\beta_{\parallel, \text{p}}} - 1 \right) (\omega \pm 1) \right) (1 + \xi_{\pm} Z(\xi_{\pm})) \right) \\ \frac{\partial \beta_{\perp, \text{p}}}{\partial \tilde{t}} &= \text{Re} \left(i \sum_{+, -} \int_{-\infty}^{\infty} d\tilde{k}_{\parallel} \frac{\delta \tilde{B}_k^2}{\tilde{k}_{\parallel}^2} \left(\frac{\beta_{\perp, \text{p}}}{\beta_{\parallel, \text{p}}} \tilde{\omega} - (\tilde{\omega}^* \mp 1) \left(\frac{\beta_{\perp, \text{p}}}{\beta_{\parallel, \text{p}}} - 1 \right) - \right. \right. \\ &\quad \left. \left. \frac{\tilde{\omega}}{\sqrt{\beta_{\parallel, \text{p}} \tilde{k}_{\parallel}}} Z(\xi_{\pm}) \left(\frac{\beta_{\perp, \text{p}}}{\beta_{\parallel, \text{p}}} (\tilde{\omega}^* - \omega \mp 2) \pm 1 - \frac{1 \mp \tilde{\omega}^*}{\tilde{\omega}} \left(\frac{\beta_{\perp, \text{p}}}{\beta_{\parallel, \text{p}}} - 1 \right) \right) \right) \right), \end{aligned} \quad (4)$$

where $\xi_{\pm} = \frac{\tilde{\omega} \pm 1}{\sqrt{\beta_{\parallel, \text{p}} \tilde{k}_{\parallel}}}$ and Z denotes the plasma dispersion function [Fried and Conte, 1961].

A self-consistent moment-kinetic solver can be constructed from Eqs. 4 by coupling them to Eq. 2 and using a bi-Maxwellian-based kinetic dispersion relation solver to update $\tilde{\omega}_k$ and $\tilde{\gamma}_k$ at each time step. We used an explicit Euler method to solve Eq. 2 and Eqs. 4, and for the dispersion relation we made use of the linear Vlasov solver DSHARK [Astfalk et al., 2015]. To perform a first validation of our full-f quasilinear kinetic solver QLEO, we benchmarked it against results from this moment-kinetic scheme. This was achieved as follows: At each time step, QLEO computes the distribution increment $\Delta \tilde{f}_{\text{p}}$ of the distribution \tilde{f}_{p} according to Eq. 1. But instead of advancing \tilde{f}_{p} by directly adding $\Delta \tilde{f}_{\text{p}}$, as would be required in the full-f approach, we compute the corresponding $\Delta \beta_{\parallel, \text{p}}$ and $\Delta \beta_{\perp, \text{p}}$ by taking the second velocity moment of $\Delta \tilde{f}_{\text{p}}$. Then, we update $\beta_{\parallel, \text{p}}$ and $\beta_{\perp, \text{p}}$ by adding $\Delta \beta_{\parallel, \text{p}}$ and $\Delta \beta_{\perp, \text{p}}$, and we reset \tilde{f}_{p} with a new bi-Maxwellian, adopting the updated $\beta_{\parallel, \text{p}}$ and $\beta_{\perp, \text{p}}$.

For the benchmark, we chose an exemplary proton firehose-unstable setup starting from a bi-Maxwellian distribution with $\beta_{\parallel, \text{p}} = 4.0$ and $T_{\perp, \text{p}}/T_{\parallel, \text{p}} = 0.5$, sampled on a parallel velocity interval $\tilde{v}_{\parallel} = [-12.0, 12.0]$ and a perpendicular velocity interval $\tilde{v}_{\perp} = [0.0, 12.0]$. We expect the electrons to not contribute much to the saturation of the PFHI, thus we keep them isotropic with $\beta_{\text{e}} = 1$. Furthermore, we assume that the Alfvén speed is much lower than the speed of light, i.e. $v_{\text{A}}/c \ll 1$.

For the resolution in time, wavenumber space, and perpendicular velocity, numerical convergence is easily achieved, while the resolution in the parallel velocity component turns out to be the main bottleneck for the numerical performance. Figure 1 shows the result of the moment-kinetic analysis for the given setups together with the outcomes of the QLEO run for different resolutions in \tilde{v}_{\parallel} . We plot the time evolution of the beta components and the total magnetic energy which is computed via

$$\delta \tilde{B}_{\text{tot}}^2 = \int d\tilde{k} \delta \tilde{B}_k^2. \quad (5)$$

As expected the moment-kinetic run shows an exponential increase of the magnetic field amplitude during the initial phase of firehose growth, followed by a saturation of the amplitudes which goes hand in hand with a reduction of the initial temperature anisotropy. In the QLEO run, a high \tilde{v}_{\parallel} -resolution is crucial to achieve good agreement with the moment-kinetic saturation curve which seems to be connected with the presence of the poles occurring in Eq. 1 for $\tilde{v}_{\parallel} = (\tilde{\omega} + 1)/\tilde{k}_{\parallel}$. While 64 points in \tilde{v}_{\perp} direction are sufficient, we have to use 8186 points in \tilde{v}_{\parallel} direction to find a satisfactory match with the outcomes of the moment-kinetic analysis over the whole simulated time interval. For lower resolutions, QLEO produces good agreement only up to a certain time whereafter it exhibits irregular behavior.

Several other setups were tested as well, yielding similar results, i.e. good agreement for high \tilde{v}_{\parallel} -resolution and partly irregular behavior for lower \tilde{v}_{\parallel} -resolution. Thus, we conclude that QLEO can successfully reproduce results of the moment-kinetic approach and we note that there is a correlation between the resolution in \tilde{v}_{\parallel} and the maximum time up to which the code gives reliable results.

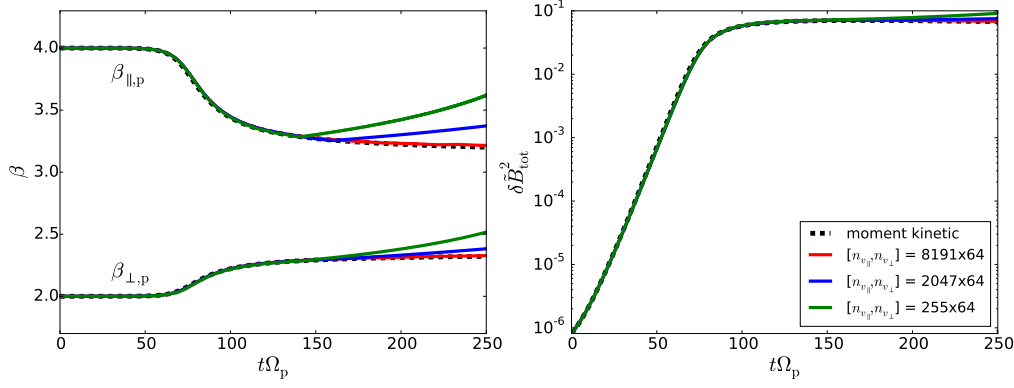


Figure 1. Results of the QLEO validation with a moment-kinetic quasilinear solver for $\beta_{\parallel,0} = 4.0$ and $T_{\perp,0}/T_{\parallel,0} = 0.5$. The figures show the time evolution of the temperature anisotropy (left) and the total magnetic energy (right) as obtained by the moment-kinetic solver and by QLEO for different parallel velocity resolutions.

3.2 Comparison with moment-kinetic analysis and hybrid-kinetic simulations

After the successful validation of QLEO with the outcomes of a moment-kinetic analysis, we now proceed by relaxing the bi-Maxwellian assumption and allowing the velocity distribution to deform during the quasilinear saturation process. For comparison, we employ the hybrid-kinetic Vlasov code HVM which simulates the fully-nonlinear dynamics of kinetic ions while the electrons are treated as a massless charge-neutralizing fluid. HVM has been developed by *Valentini et al.* [2007] and is based on *Mangeney et al.* [2002]. In the considered PFHI setups, electron-kinetic effects are expected to be insignificant, thus, the hybrid-kinetic scheme appears to be an appropriate choice. However, since the expected length and time scales are close to ion inertial scales, the Hall term is included in the Ohm's law that governs the fluid electrons, i.e. HVM is used in its *HMHD limit* (Eq. 9 in *Valentini et al.* [2007]). In HVM, we use a one-dimensional spatial grid with periodic boundary conditions which is aligned with a background magnetic field in order to allow for parallel wave propagation. The velocity space is three-dimensional and the simulation is initialized with bi-Maxwellian velocity distributions with selected initial β_{\parallel} and β_{\perp} .

The QLEO runs were performed for six different one-dimensional firehose-unstable setups. We studied three cases, (I)–(III), with similar growth rates, $\tilde{\gamma}_{\max} \sim 0.04$, to check applicability for various $\beta_{\parallel,p}$. And in the setups (III)–(VI), we compared four cases with fixed $\beta_{\parallel,p} = 4.0$ to study the effect of varying initial anisotropies. Due to numerical constraints, we were restricted to using a comparably low number of grid points in parallel velocity space. In most cases, we found $n_{\parallel} = 255$ and $n_{\perp} = 64$ to be a reasonable trade-off between computing time and reliability of the results. A summary of the setups and the used parameters can be found in table 3.2.

In figures 2–7, we compare the QLEO results for setups (I)–(VI) with the corresponding moment-kinetic analysis and the 1D3V HVM simulations.

The beta components for the QLEO runs and in the HVM simulations are obtained by numerically computing the second velocity moment of the distribution function at each time step. Similar to the QLEO runs in section 3.1 where we observed a sudden transition from regular to irregular behavior at a certain time which was correlated with the number of grid points in \tilde{v}_{\parallel} , we again encountered difficulties in the $\Delta \tilde{f}_p$ estimation which were clearly related to the low \tilde{v}_{\parallel} -resolution. Thus, we only show the QLEO curves up to a maximum time within which they appear to be reliable.

	$\beta_{\parallel,p}$	$T_{\perp,p}/T_{\parallel,p}$	n_{\parallel}	n_{\perp}	\tilde{v}_{\parallel}	\tilde{v}_{\perp}	$\tilde{\gamma}_{\max}$
I	15.0	0.847	255	64	$[-24.0, 24.0]$	$[0.0, 22.0]$	0.041
II	10.0	0.794	255	128	$[-20.0, 20.0]$	$[0.0, 18.0]$	0.041
III	4.0	0.588	255	64	$[-12.0, 12.0]$	$[0.0, 12.0]$	0.039
IV	4.0	0.630	255	64	$[-12.0, 12.0]$	$[0.0, 12.0]$	0.021
V	4.0	0.500	255	64	$[-12.0, 12.0]$	$[0.0, 12.0]$	0.085
VI	4.0	0.425	255	64	$[-12.0, 12.0]$	$[0.0, 8.0]$	0.120

Table 1. QLEO velocity distribution parameters for the six setups used in the full-f analysis and the corresponding initial maximum growth rates.

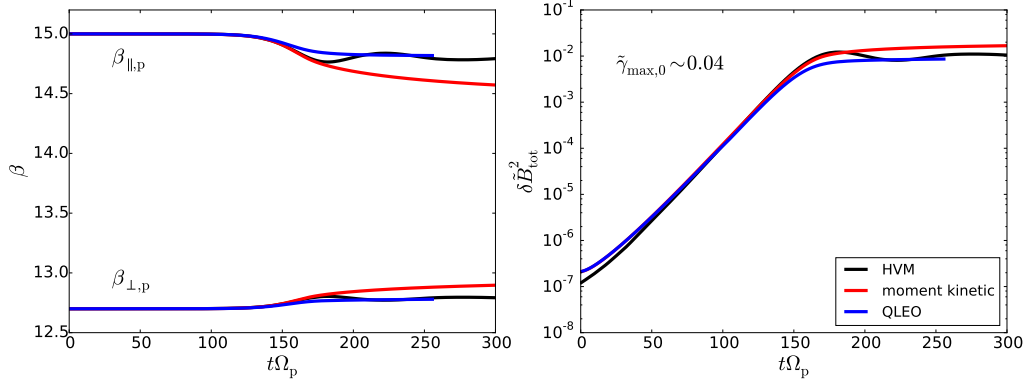


Figure 2. Results of the QLEO runs for setup (I) with initial parallel beta $\beta_{\parallel,0} = 15.0$ and anisotropy $T_{\perp,0}/T_{\parallel,0} = 0.847$, compared to the outcomes of a moment-kinetic analysis and hybrid-kinetic simulations with HVM. The figures show the time evolution of the temperature anisotropy (left) and the total magnetic energy (right).

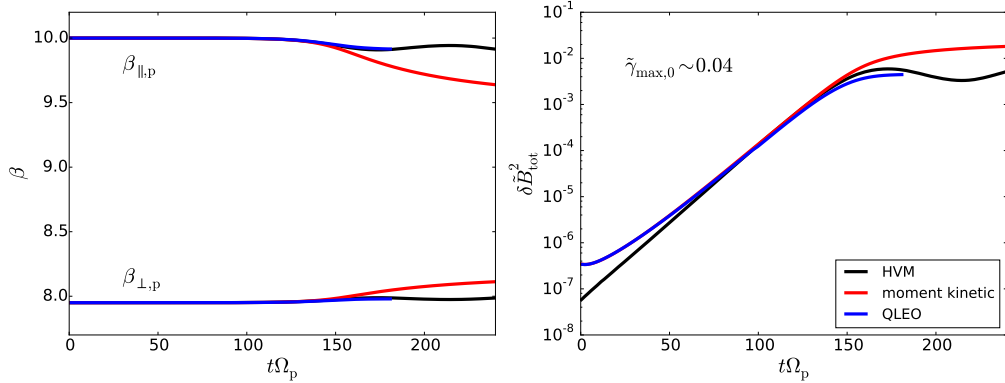


Figure 3. Results of the QLEO runs for setup (II) with initial parallel beta $\beta_{\parallel,0} = 10.0$ and anisotropy $T_{\perp,0}/T_{\parallel,0} = 0.794$, compared to the outcomes of a moment-kinetic analysis and hybrid-kinetic simulations with HVM. The figures show the time evolution of the temperature anisotropy (left) and the total magnetic energy (right).

In the high-anisotropy setups (V) and (VI), shown in figures 6 and 7, an accurate comparison with the HVM simulation results is difficult due to the strong oscillatory behavior of the beta components and the magnetic energy, indicating significant particle trapping which is not accounted for in the quasilinear approach. However, to guide the

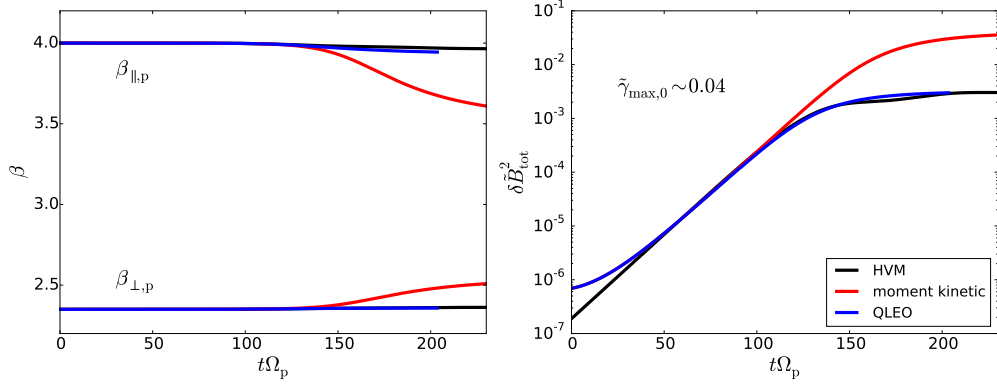


Figure 4. Results of the QLEO runs for setup (III) with initial parallel beta $\beta_{\parallel,0} = 4.0$ and anisotropy $T_{\perp,0}/T_{\parallel,0} = 0.588$, compared to the outcomes of a moment-kinetic analysis and hybrid-kinetic simulations with HVM. The figures show the time evolution of the temperature anisotropy (left) and the total magnetic energy (right).

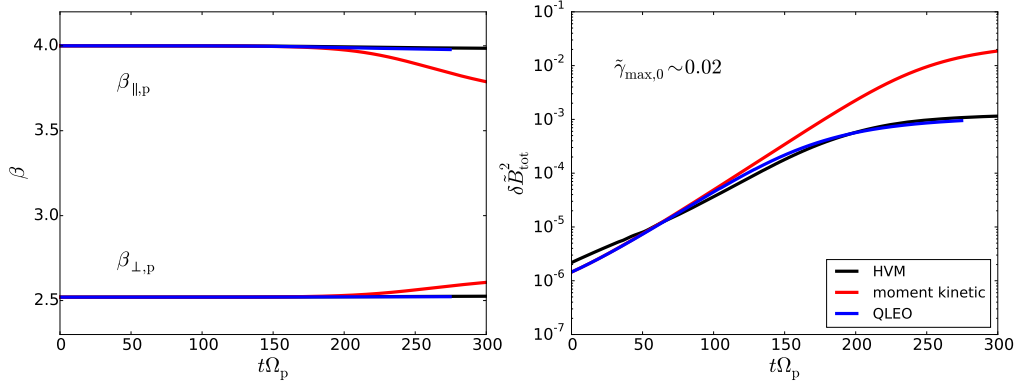


Figure 5. Results of the QLEO runs for setup (IV) with initial parallel beta $\beta_{\parallel,0} = 4.0$ and anisotropy $T_{\perp,0}/T_{\parallel,0} = 0.630$, compared to the outcomes of a moment-kinetic analysis and hybrid-kinetic simulations with HVM. The figures show the time evolution of the temperature anisotropy (left) and the total magnetic energy (right).

eye we inserted the average beta components and magnetic energy levels in the saturation stage as dashed lines.

In agreement with *Seough et al.* [2015], we find that the moment-kinetic analysis yields good agreement with the outcomes of hybrid-kinetic simulations for higher $\beta_{\parallel,p}$ while it overpredicts the anisotropy reduction and the saturation energy levels for lower $\beta_{\parallel,p}$. Especially the setups (III)–(VI) with $\beta_{\parallel,p} = 4.0$, shown in figures 4–7, exhibit clear offsets between the simulation outcomes and the moment kinetic computations. In comparison, the full-f approach appears to give good results for both low and high $\beta_{\parallel,p}$. In all scenarios, it yields a less-pronounced temperature anisotropy reduction than the moment-kinetic approach and, except for the high-growth-rate setup (VI), shown in figure 7, gives good overall-agreement with the final saturation levels in both the beta components and the magnetic field amplitude, even for setup (V), shown in figure 6, where noticeable particle trapping is present. Comparing setups (III)–(VI), shown in figures 4–7, we also note that the agreement with the simulation outcomes seems to correlate with the strength of the initial anisotropy. We observe better agreement for weaker firehose growth where almost no pressure anisotropy reduction is present, while for higher initial anisotropies

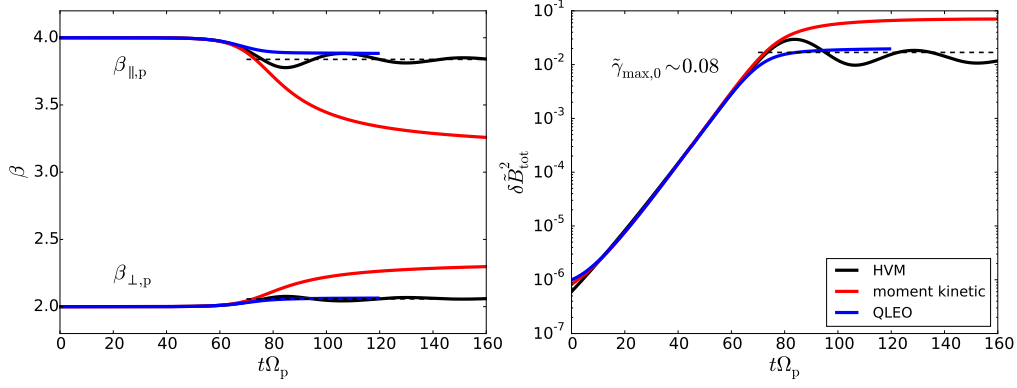


Figure 6. Results of the QLEO runs for setup (V) with initial parallel beta $\beta_{\parallel,0} = 4.0$ and anisotropy $T_{\perp,0}/T_{\parallel,0} = 0.500$, compared to the outcomes of a moment-kinetic analysis and hybrid-kinetic simulations with HVM. The figures show the time evolution of the temperature anisotropy (left) and the total magnetic energy (right). The dashed lines mark the estimated average of the final anisotropy and magnetic energy levels of the HVM simulation.

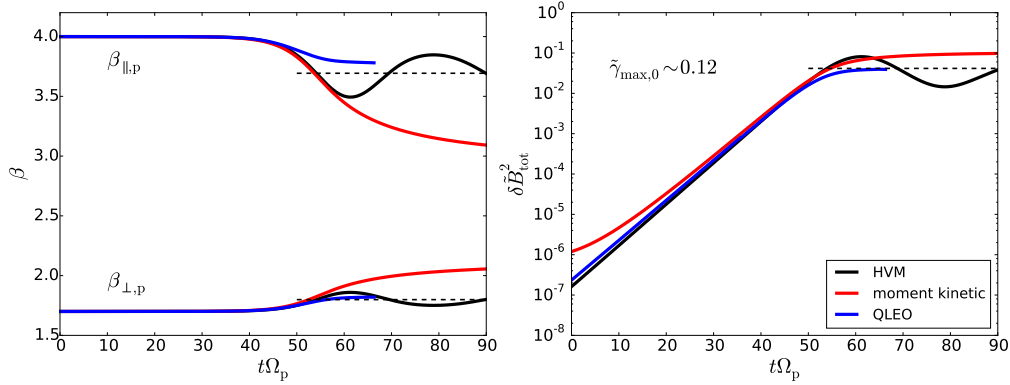


Figure 7. Results of the QLEO runs for setup (VI) with initial parallel beta $\beta_{\parallel,0} = 4.0$ and anisotropy $T_{\perp,0}/T_{\parallel,0} = 0.425$, compared to the outcomes of a moment-kinetic analysis and hybrid-kinetic simulations with HVM. The figures show the time evolution of the temperature anisotropy (left) and the total magnetic energy (right). The dashed lines mark the estimated average of the final anisotropy and magnetic energy levels of the HVM simulation.

(setup (V) and setup (VI)), the hybrid-kinetic simulations exhibit increasingly stronger reduction of the temperature anisotropy than the quasilinear model. Possible explanations for this discrepancy will be discussed in section 4.

The reason why the full-f approach gives less pronounced temperature anisotropy reduction than the moment-kinetic approach can be inferred from figures 8 and 9 which show exemplary snapshots of the velocity distribution taken from the QLEO runs for the high- β_{\parallel} setup (I) and the low- β_{\parallel} setup (V). In both scenarios, the initially bi-Maxwellian distribution (dashed contours) is deformed by cyclotron-resonant diffusion. In setup (I) which has $\beta_{\parallel} = 15.0$, the deformation is more pronounced than in setup (V) which has $\beta_{\parallel} = 4.0$. This may explain why in setup (I) the moment-kinetic approach agrees better with QLEO and HVM than in setup (V). Qualitatively, the distribution deformation can be understood as follows: When undergoing cyclotron-resonant interaction with a wave, the particles conserve their energy in a reference frame co-moving with the wave's

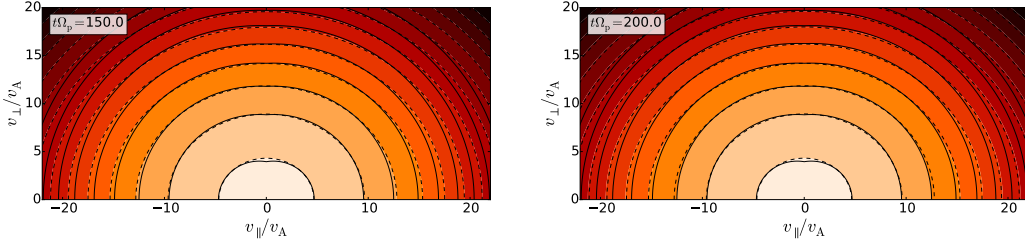


Figure 8. Snapshots of the velocity distribution from the QLEO run of setup (I) with $\beta_{\parallel,0} = 15.0$ and $T_{\perp,0}/T_{\parallel,0} = 0.847$ at different points in time (filled contours). The dashed lines show the contours of a reference bi-Maxwellian distribution with $\beta_{\parallel,p}$ and $\beta_{\perp,p}$ at the given point in time. The solid contours mark the single wave characteristics of the fastest growing mode in the system, according to Eq. 6.

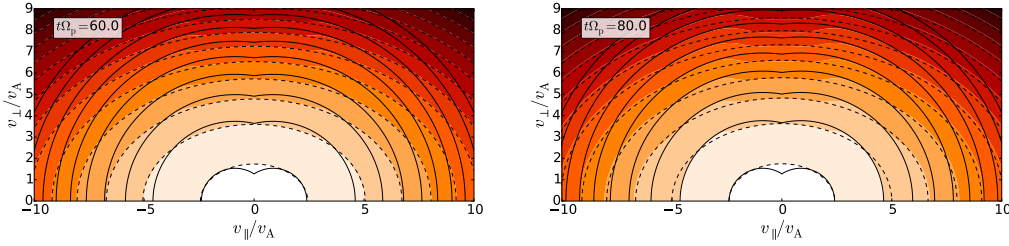


Figure 9. Snapshots of the velocity distribution from the QLEO run of setup (V) with $\beta_{\parallel,0} = 4.0$ and $T_{\perp,0}/T_{\parallel,0} = 0.5$ at different points in time (filled contours). The dashed lines show the contours of a reference bi-Maxwellian distribution with $\beta_{\parallel,p}$ and $\beta_{\perp,p}$ at the given point in time. The solid contours mark the single wave characteristics of the fastest growing mode in the system, according to Eq. 6.

phase speed (see, e.g., *Kennel and Engelmann* [1966]). In the limit of weak growth or damping, this condition yields the conservation equation

$$\tilde{v}_{\perp}^2 + \left(\tilde{v}_{\parallel} - \frac{\tilde{\omega}_k}{\tilde{k}_{\parallel}} \right)^2 \approx \text{const.} \quad (6)$$

The solid lines in figures 8 and 9 illustrate the contours obeying the conservation equation for the dominant mode in the system, i.e. the mode which initially exhibits the strongest growth. These contours are also referred to as *single wave characteristics*. Since the fastest growing mode dominates the cyclotron-resonant diffusion in the system, the particles are expected to mainly diffuse along these contours. They tend to erase gradients along the single wave characteristics which explains why the resonant peaks of the velocity distribution in figures 8 and 9 align with the corresponding contours. And since in figure 8 the single wave characteristics roughly follow the bi-Maxwellian contours only weakly non-Maxwellian deformation occurs which justifies a good applicability of the moment-kinetic approach. A clear signature of cyclotron-resonant diffusion is also observed in the HVM simulations, as has already been demonstrated for setup (V) in *Astfalk and Jenko* [2017].

The complex non-Maxwellian shape of the velocity distributions at later times also yields more complex dispersion curves. In figures 10 and 11, we compare dispersion curves from the quasilinear full-f approach, the moment-kinetic approach, and the HVM simulation for setup (V). Please note that due to too-low resolution the HVM dispersion curves in figure 11 are not obtained from direct Fourier analysis of the fluctuation spectra but

instead they are produced by feeding gyro-averaged velocity distributions from the HVM simulations into the dispersion relation solver LEOPARD.

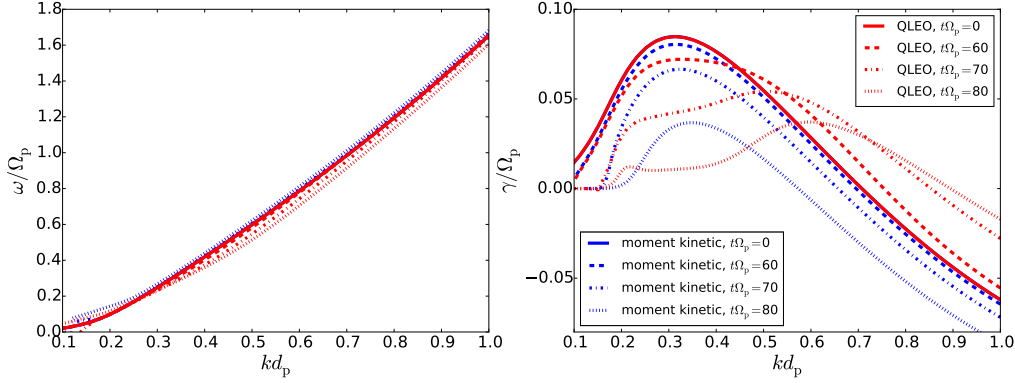


Figure 10. Dispersion relations taken from the QLEO runs of setup (V) at different points in time, compared to the corresponding moment kinetic results.

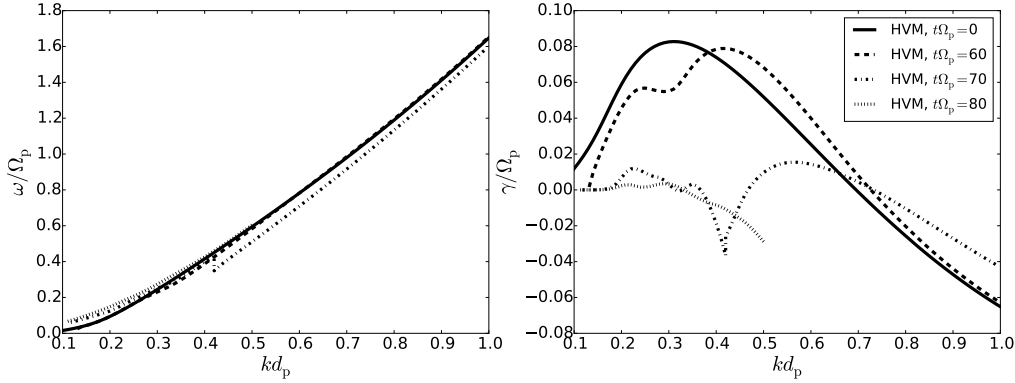


Figure 11. Dispersion relations based on the gyro-averaged velocity distributions taken from the HVM runs of setup (V) at different points in time.

From the red curves in figure 10, we infer that during the firehose saturation in the QLEO run the unstable wavenumber range is slowly extending towards higher and higher \tilde{k}_{\parallel} . At the same time, the low- \tilde{k}_{\parallel} modes get stabilized. Furthermore, while the velocity distribution aligns with the single wave characteristics of the most unstable mode, a strong suppression sets in around this mode which first leads to a flattening of the growth peak and later causes the formation of a plateau and a two-growth-peak structure. Meanwhile, the real frequencies stay mostly unaffected which is expected since they do not depend on the detailed structure but only on the gross properties of the velocity distribution.

Similar to the full-f analysis, the moment-kinetic run (blue curves in figure 10) also exhibits a stabilization of the low- \tilde{k}_{\parallel} modes. For both approaches, the growth rates of these modes evolve in the same way, it is only later that they start to deviate. For modes with $\tilde{k}_{\parallel} \lesssim 0.2$, we expect high parallel resonance velocities $\tilde{v}_{\text{res}} \gtrsim 6.0$. In figure 9, we notice that at such high parallel velocities there is only weak deviation from a bi-Maxwellian distribution, thus explaining the similar early evolution of the modes. For high- \tilde{k}_{\parallel} modes, which resonate with particles at lower parallel velocities, stronger deviations between the two approaches are expected and observed. For the moment kinetic analysis, we do not

see an extension of the unstable wavenumber range to higher \tilde{k}_{\parallel} but a shrinking to smaller \tilde{k}_{\parallel} . Also, there is no formation of a low-growth-rate plateau which, in the full-f analysis, was apparently caused by the strong cyclotron-resonant diffusion.

The evolution of the dispersion properties based on velocity distributions extracted from the hybrid-kinetic simulation and depicted in figure 11, shows similarities with the foregoing but also some obvious discrepancies. During the firehose saturation in the HVM run, the unstable wavenumber range again stretches out to higher \tilde{k}_{\parallel} while the growth at low \tilde{k}_{\parallel} gets suppressed. Also, we observe the development of a two-growth-peak structure. However, the growth suppression happens more quickly, reducing the growth rates faster than in the quasilinear full-f scenario. Also, we do not see the formation of a low-growth-rate plateau. Instead, the structure of the dispersion curve assumes a more complex shape in the later stage. Around $\tilde{t} = 70.0$ and $\tilde{k}_{\parallel} \sim 0.4$, the unstable branch splits into two, yielding a branch with a low- \tilde{k}_{\parallel} growth peak and one with a high- \tilde{k}_{\parallel} growth peak which exhibits a somewhat lower frequency than the corresponding branches at earlier times. Later, the growth peak at high \tilde{k}_{\parallel} gets strongly damped away and only the low- \tilde{k}_{\parallel} branch still shows weak instability which eventually disappears for $\tilde{t} \gtrsim 80.0$, while at the same time the QLEO runs still exhibit significant growth. The implications of the observed discrepancies are briefly discussed in section 4.

Finally, to examine the validity of our numerical scheme, we analyzed the conservation properties for our different setups. The closed system, Eqs. 1 and 2, obeys an energy conservation law in the form of

$$\frac{d}{dt} (\beta_{\perp,p} + 0.5\beta_{\parallel,p} + \delta B_{\text{tot}}^2) = 0. \quad (7)$$

In setups (I)–(V), we find that the total energy in the systems is well conserved within a limit of $< 0.5\%$ while in setup (VI) the energy increases by $\sim 6\%$.

4 Discussion and conclusion

It has long been known that despite its traditional reputation of being a macroscopic fluid-like instability, the PFHI often requires a fully-kinetic treatment. While for $\beta_{\parallel,p} \gg 1$, the fluid approximation may be applicable, the regime $\beta_{\parallel,p} \lesssim 25$, which is especially relevant for the solar wind, asks for a careful inclusion of particle resonance effects.

As long as we are only concerned with the linear dispersion properties of a firehose-unstable system, the step from a macroscopic to a microscopic picture is an easy one since existing numerical dispersion relation solvers can be employed to overcome the non-analytic nature of kinetic theory. However, if the growth saturation of the firehose instability is to be studied in the framework of quasilinear theory, a fully-kinetic treatment is challenging which is why standard textbooks and classic monographs consider the quasilinear firehose saturation in the fluid limit only.

Seough et al. [2015] went beyond the traditional fluid ansatz by numerically solving the self-consistent set of kinetic quasilinear equations for various firehose-unstable systems. However, their investigations were restricted to a moment-kinetic approach where the bi-Maxwellian shape of the distribution is preserved throughout the saturation process. This limitation, which was necessary to simplify the numerical treatment, obscured to which extent the PFHI saturation can be understood in the limits of QLT or whether other nonlinear effects have to be taken into account too. We lifted this limitation by allowing for a non-Maxwellian deformation of the velocity distribution.

We applied the moment-kinetic and a full-f approach to six firehose-unstable setups and compared the predicted temperature anisotropy reduction and magnetic energy saturation levels to outcomes of fully-nonlinear hybrid-kinetic simulations. While the moment-kinetic analysis showed an increasing offset for decreasing $\beta_{\parallel,p}$, the QLEO code produced good agreement also in the low- $\beta_{\parallel,p}$ regime as long as the initial anisotropy was not too high.

However, when comparing the temporal changes in the dispersion properties of the quasilinear full-f runs and the HVM simulations for the intermediate-growth setup (V), we found that in the fully-nonlinear hybrid-kinetic model the firehose growth was suppressed faster than in the QLEO runs. Although not reported here, we found a similar discrepancy also for the lowest-anisotropy scenario, setup (IV). This suggests that QLT does not fully cover the microscopic physics that governs the firehose growth suppression even for cases which show otherwise excellent agreement for the saturation levels of the macroscopic beta components and the magnetic energy between QLEO and the hybrid-kinetic simulations. The good agreement may be explained by the fact that the initially most unstable mode strongly dominates the cyclotron-resonant diffusion and the subsequent changes in the dispersion properties during the saturation process only slightly modulate the shaping of the velocity distribution.

In contrast to the setups (I)–(V), the pressure anisotropy reduction in the high-anisotropy case, setup (VI), with initial maximum growth rate $\tilde{\gamma}_{\max} = 0.12$, showed noticeable disagreement between the QLEO results and the hybrid-kinetic simulations. We found that the total energy in this setup is not as well conserved as in the other cases which points to a failure of the numerical scheme. However, we suggest that the problem may also be due to a failure of the QLT model itself. As a weak turbulence theory, the model applies only when the amplitude of the electromagnetic fluctuations in the system is small compared to the thermal energy of the plasma. In the considered setup, the ratio $\delta B_k^2/E_{\text{therm}}$ reached a level of $\sim 2\%$ which does not seem to strongly violate the assumption. However, nonlinear wave-wave coupling may be triggered by the modes with highest amplitudes, disrupting the quasilinear approximation. Looking at the time evo-

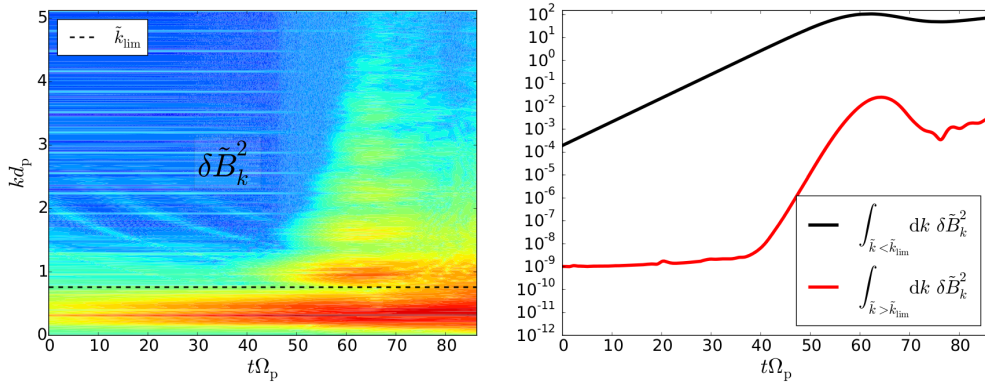


Figure 12. Time evolution of the magnetic energy spectrum (left) and the contribution of low- and high-k modes (right), observed in the HVM simulations of the high-anisotropy setup (VI). The wavenumber \tilde{k}_{lim} separates the initially unstable (low-k) from the initially stable (high-k) part of the spectrum.

lution of the magnetic energy spectrum taken from the HVM simulations of setup (VI), shown in figure 12 (left), we see that after the modes in the unstable wavenumber range have grown to high-enough amplitudes, nonlinear wave-wave coupling leads to the formation of sidebands at higher wavenumbers which are (odd) harmonics of the initially unstable wavenumber range. In figure 12 (right), we compare the magnetic energy in the initially unstable wavenumber range with the energy content in modes with higher wavenumbers. We observe a strong growth in the high-k energy which is connected with the appearing sidebands. However, the growth saturates well below the energy level of the low-k modes which may suggest that this effect only slightly modulates the dynamics in the

system. However, studying the relative importance of nonlinear wave-wave coupling is beyond the scope of this work but may be addressed systematically in a future project.

Another limitation of QLT is that of slow temporal changes in the distribution function, i.e.

$$\delta \sim \frac{1}{f_0} \frac{df_0}{dt} / \gamma_{\max} \ll 1. \quad (8)$$

For setup (VI), we estimated $\delta \sim 10\%$ which appears to be a more severe violation than the foregoing. For the setups (I)–(IV), we find $\delta \sim 0.1\%$, for the setup (V) we have $\delta \sim 1\%$. Also, setup (VI) showed significant particle trapping which further violates the quasilinear approximation. Thus, the high-anisotropy setup (VI) may indeed be outside the range of validity of QLT. We conclude that kinetic QLT is a valid approach for modeling the temperature anisotropy reduction only if the initial firehose instability growth is not too strong.

Finally, our findings also confirm the results of *Astfalk and Jenko* [2017], namely that for $\beta_{\parallel,p} \sim \mathcal{O}(1)$, strong cyclotron-resonant scattering is a main driver for the firehose stabilization, which is why the moment-kinetic approach fails in this regime since it cannot properly account for the distribution deformation due to the resonant diffusion. At the same time, the reduction of the macroscopic temperature anisotropy is relatively weak which indicates that in the solar wind the PFHI may not be the dominant player in constraining the anisotropy when $2 \lesssim \beta_{\parallel,p} \lesssim 10$. However, being restricted to a one-dimensional analysis, we can gain only limited insight into the challenging problem of temperature anisotropy regulation in the solar wind. In a two-dimensional setup, PFHI modes with different propagation angles can grow simultaneously which yields more complex diffusion dynamics. The presence of obliquely propagating waves is expected to enhance the diffusion [*Karimabadi et al.*, 1992], causing a stronger anisotropy reduction [*Gary et al.*, 1998]. This is further complicated by the fact that the OFHI may be excited as well which *Hellinger and Trávníček* [2008] found to be a very efficient mechanism for temperature anisotropy reduction. The competition between the PFHI and the OFHI has been studied in *Hellinger and Matsumoto* [2001] with two-dimensional hybrid-kinetic simulations. In this work, the nonlinear evolution of the OFHI was observed to behave in a rather non-quasilinear manner, as was also found in *Hellinger and Matsumoto* [2000]. Thus, even a two-dimensional generalization of the presented quasilinear full-f approach may be of very limited applicability in such more realistic scenarios.

Similarly, the competition between the EMIC instability and the mirror instability which is driven by the opposite temperature anisotropy, $T_{\perp,p} > T_{\parallel,p}$, may be out of reach for such a scheme. However, due to the apparent similarities between the PFHI and the EMIC instability the presented quasilinear scheme promises to give interesting insights into the EMIC instability saturation in a purely parallel setup. This may be addressed in a follow-up project.

A: Meaning of the quantities and used normalizations

The velocity components parallel and perpendicular to the background magnetic field B_0 , i.e. v_{\parallel} and v_{\perp} , are normalized according to $\tilde{v} = v/v_A$ with the Alfvén velocity $v_A = B_0/\sqrt{4\pi n_p m_p}$ where n_p is the proton number density and m_p is the proton mass. For the (complex) frequency we use $\tilde{\omega} = (\omega_k + i\gamma_k)/\Omega_p$ with the proton gyro frequency $\Omega_p = eB_0/m_p c$ where e denotes the proton’s charge. The time is also normalized with respect to the proton gyro frequency, i.e. $\tilde{t} = t\Omega_p$. The parallel wavenumber is given in units of the proton inertial length $d_p = v_A/\Omega_p$ such that $\tilde{k}_{\parallel} = k_{\parallel} d_p$. For the magnetic energy in each mode, we write $\delta \tilde{B}_k^2 = \delta B_k^2/B_0^2 d_p$. The velocity distribution is normalized with respect to $\tilde{f}_p = f_p v_A^3/n_p$.

Acknowledgments

We warmly acknowledge F. Califano for providing access to the HVM code. Furthermore, we thank D. Jarema and A. Ross for fruitful discussions and J. Seough for his helpful

comments. The numerical data used for generating the presented figures is available via https://osf.io/nd7ap/?view_only=5bff2b87411f49d180a53204e52da887. The linear dispersion relation solver LEOPARD can be found on <https://github.com/pastfalk/LEOPARD>. The presented quasilinear solver QLEO and the used moment kinetic solver can be obtained from the corresponding author. Finally, we thank the referees for their efforts in improving the quality of this work.

References

- Astfalk, P., and F. Jenko (2017), LEOPARD: A grid-based dispersion relation solver for arbitrary gyrotropic distributions, *Journal of Geophysical Research (Space Physics)*, *122*, 89–101, doi:10.1002/2016JA023522.
- Astfalk, P., T. Görler, and F. Jenko (2015), DSHARK: A dispersion relation solver for obliquely propagating waves in bi-kappa-distributed plasmas, *Journal of Geophysical Research (Space Physics)*, *120*, 7107–7120, doi:10.1002/2015JA021507.
- Bale, S. D., J. C. Kasper, G. G. Howes, E. Quataert, C. Salem, and D. Sundkvist (2009), Magnetic Fluctuation Power Near Proton Temperature Anisotropy Instability Thresholds in the Solar Wind, *Physical Review Letters*, *103*(21), 211101, doi:10.1103/PhysRevLett.103.211101.
- Chen, C. H. K., L. Matteini, A. A. Schekochihin, M. L. Stevens, C. S. Salem, B. A. Maruca, M. W. Kunz, and S. D. Bale (2016), Multi-species Measurements of the Firehose and Mirror Instability Thresholds in the Solar Wind, *The Astrophysical Journal Letters*, *825*, L26, doi:10.3847/2041-8205/825/2/L26.
- Davidson, R. C. (1972), *Methods in nonlinear plasma theory.*, New York, NY (USA): Academic Press.
- Davidson, R. C., and H. J. Völk (1968), Macroscopic Quasilinear Theory of the Garden-Hose Instability, *Physics of Fluids*, *11*, 2259–2264, doi:10.1063/1.1691810.
- Fried, B. D., and S. D. Conte (1961), *The Plasma Dispersion Function*, New York: Academic Press, 1961.
- Gary, S. P., and M. A. Lee (1994), The ion cyclotron anisotropy instability and the inverse correlation between proton anisotropy and proton beta, *Journal of Geophysical Research*, *99*, 11,297–11,302, doi:10.1029/94JA00253.
- Gary, S. P., H. Li, S. O'Rourke, and D. Winske (1998), Proton resonant firehose instability: Temperature anisotropy and fluctuating field constraints, *Journal of Geophysical Research*, *103*, 14,567–14,574, doi:10.1029/98JA01174.
- Gary, S. P., R. M. Skoug, J. T. Steinberg, and C. W. Smith (2001), Proton temperature anisotropy constraint in the solar wind: ACE observations, *Geophysical Research Letters*, *28*, 2759–2762, doi:10.1029/2001GL013165.
- Hellinger, P., and H. Matsumoto (2000), New kinetic instability: Oblique Alfvén fire hose, *Journal of Geophysical Research*, *105*, 10,519–10,526, doi:10.1029/1999JA000297.
- Hellinger, P., and H. Matsumoto (2001), Nonlinear competition between the whistler and Alfvén fire hoses, *Journal of Geophysical Research*, *106*, 13,215–13,218, doi:10.1029/2001JA000026.
- Hellinger, P., and P. M. Trávníček (2008), Oblique proton fire hose instability in the expanding solar wind: Hybrid simulations, *Journal of Geophysical Research (Space Physics)*, *113*, A10109, doi:10.1029/2008JA013416.
- Hellinger, P., P. Trávníček, J. C. Kasper, and A. J. Lazarus (2006), Solar wind proton temperature anisotropy: Linear theory and WIND/SWE observations, *Geophysical Research Letters*, *33*, L09101, doi:10.1029/2006GL025925.
- Isenberg, P. A., B. A. Maruca, and J. C. Kasper (2013), Self-consistent Ion Cyclotron Anisotropy-Beta Relation for Solar Wind Protons, *The Astrophysical Journal*, *773*, 164, doi:10.1088/0004-637X/773/2/164.
- Karimabadi, H., D. Krauss-Varban, and T. Terasawa (1992), Physics of pitch angle

- scattering and velocity diffusion. I - Theory, *Journal of Geophysical Research*, *97*, 13, doi:10.1029/92JA00997.
- Kasper, J. C., A. J. Lazarus, and S. P. Gary (2002), Wind/SWE observations of firehose constraint on solar wind proton temperature anisotropy, *Geophysical Research Letters*, *29*, 1839, doi:10.1029/2002GL015128.
- Kennel, C. F., and F. Engelmann (1966), Velocity Space Diffusion from Weak Plasma Turbulence in a Magnetic Field, *Physics of Fluids*, *9*, 2377–2388, doi: 10.1063/1.1761629.
- Landau, L. D. (1946), On the vibrations of the electronic plasma, *Yad. Fiz.*, *10*, 25.
- Mangeney, A., F. Califano, C. Cavazzoni, and P. Travnicek (2002), A Numerical Scheme for the Integration of the Vlasov-Maxwell System of Equations, *Journal of Computational Physics*, *179*, 495–538, doi:10.1006/jcph.2002.7071.
- Matteini, L., S. Landi, P. Hellinger, and M. Velli (2006), Parallel proton fire hose instability in the expanding solar wind: Hybrid simulations, *Journal of Geophysical Research (Space Physics)*, *111*, A10101, doi:10.1029/2006JA011667.
- Matteini, L., P. Hellinger, S. Landi, P. M. Trávníček, and M. Velli (2012), Ion Kinetics in the Solar Wind: Coupling Global Expansion to Local Microphysics, *Space Science Reviews*, *172*, 373–396, doi:10.1007/s11214-011-9774-z.
- Michno, M. J., M. Lazar, P. H. Yoon, and R. Schlickeiser (2014), Effects of Electrons on the Solar Wind Proton Temperature Anisotropy, *The Astrophysical Journal*, *781*, 49, doi:10.1088/0004-637X/781/1/49.
- Quest, K. B., and V. D. Shapiro (1996), Evolution of the fire-hose instability: Linear theory and wave-wave coupling, *Journal of Geophysical Research*, *101*, 24,457–24,470, doi:10.1029/96JA01534.
- Sagdeev, R., and V. Shafranov (1961), On the instability of a plasma with an anisotropic distribution of velocities in a magnetic field, *Soviet Physics JETP*, *12*(1).
- Seough, J., and P. H. Yoon (2012), Quasilinear theory of anisotropy-beta relations for proton cyclotron and parallel firehose instabilities, *Journal of Geophysical Research (Space Physics)*, *117*, A08101, doi:10.1029/2012JA017645.
- Seough, J., P. H. Yoon, and J. Hwang (2014), Quasilinear theory and particle-in-cell simulation of proton cyclotron instability, *Physics of Plasmas*, *21*(6), 062118, doi:10.1063/1.4885359.
- Seough, J., P. H. Yoon, and J. Hwang (2015), Simulation and quasilinear theory of proton firehose instability, *Physics of Plasmas*, *22*(1), 012303, doi: 10.1063/1.4905230.
- Shaaban, S. M., M. Lazar, S. Poedts, and A. Elhanbaly (2017), Shaping the solar wind temperature anisotropy by the interplay of electron and proton instabilities, *Astrophysics and Space Science*, *362*, 13, doi:10.1007/s10509-016-2994-7.
- Shapiro, V., and V. Shevchenko (1964), Quasilinear theory of instability of a plasma with an anisotropic ion velocity distribution, *Sov. Phys. JETP*, *18*, 1109–1116.
- Southwood, D. J., and M. G. Kivelson (1993), Mirror instability. I - Physical mechanism of linear instability, *Journal of Geophysical Research*, *98*, 9181–9187, doi: 10.1029/92JA02837.
- Valentini, F., P. Trávníček, F. Califano, P. Hellinger, and A. Mangeney (2007), A hybrid-Vlasov model based on the current advance method for the simulation of collisionless magnetized plasma, *Journal of Computational Physics*, *225*, 753–770, doi:10.1016/j.jcp.2007.01.001.
- Yoon, P. H. (1995), Garden-hose instability in high-beta plasmas, *Physica Scripta Volume T*, *60*, 127–135, doi:10.1088/0031-8949/1995/T60/016.
- Yoon, P. H., J. Seough, and R. Gaerzler (2014), Temperature Anisotropy Upper Bounds and Low-Frequency Electromagnetic Fluctuations in the Solar Wind, in *Outstanding Problems in Heliophysics: From Coronal Heating to the Edge of the Heliosphere*, *Astronomical Society of the Pacific Conference Series*, vol. 484,

edited by Q. Hu and G. P. Zank, p. 248.